Elemental Analysis of the Jarosites and the Consequences for the magnetism

William G. Bisson and Andrew S. Wills

Department of Chemistry, UCL, Christopher Ingold Laboratories,

20 Gordon Street, London, UK, WC1H 0AJ

November 7, 2007

Abstract

Highly frustrated systems have degenerate ground states that lead to novel properties. In magnetism its consequences underpin exotic and technologically important effects: high temperature superconductivity, colossal magnetoresistence, and the anomalous Hall effect. One of the enduring mysteries of highly frustrated magnetism is why certain experimental systems have a spin glass transition that it is not determined by the strength of the dominant magnetic interactions. There have been suggestions that some real materials possess disorder of the magnetic sites or bonds that is responsible for the glassy behaviour. This work shows that the spin glass transition in the model *kagomé* antiferromagnet hydronium jarosite arises not from random disorder and that the intrinsic magnetic properties of this *kagomé* system are robust to site disorder. This simplifies markedly the treatment of the complex spin glass dynamics and has implications far beyond magnetism, as spin glasses provide important models for the out-of-equilibrium dynamics in other frustrated systems, including proteins and neural networks.

1   Introduction

The jarosite minerals have been extensively researched in two primary fields: frustrated magnetism[1] and acid mine drainage (AMD),[2,3] though at no point has there been a total convergence between the two disciplines. In nature, jarosites occur through the weathering process of Pyrite, FeS, as high concentrations of Fe^{2+} are released from the dissolution of FeS that decreases the pH of the local water area. Through either microbial action or dissolved oxygen, the Fe^{2+} oxidises to Fe^{3+}.[4-8] Around these Fe^{3+} centres chains of hydroxysulphates attach themselves to form the characteristic iron flocs.[9] Extremely low values of pH and the incorporation of a suitably sized cation will cause jarosite precipitation with the following formula: $A_{1-x}(H_3O)_x Fe_{3-y}(SO_4)_2(OH)_{6-3y}(H_2O)_{3y}$, where A=$K^+$, Na^+, Ag^+, Rb^+, NH_4^+, H_3O^+, Pb^{2+}, Tl^{2+}.[4-8] The high water content and the low temperature formation conditions in nature can lead to a large deviation from the ideal stoichiometry. Naturally occurring jarosites may be charged balanced by the incorporation of other cations in the B site which

are not trivalent cations,[10] such as copper or zinc leading to the formation of other minerals.[11] If there are Fe deficiencies, charge balancing requires the replacement of an A-site with a H_2O unit or protonation of the bridging OH. Likewise, increasing incorporation of water into the structure will be charged balanced by Fe vacancies.[3,7,8,12]

AMD research has centered on jarosite formation at relatively low temperatures (below 100°C), in very low pH, (pH < 2), aqueous media, and to exploit the unstoichiometry that allows the structure to uptake toxic metal ions such as Tl^{2+}, Pb^{2+}, Se^{6+}, As^{3+}; and Cr^{6+}. There have been many methods to produce jarosites synthetically to investigate and exploit this unstoichiometric nature.[8,11,12] Primarily researched for mining purposes to either remove unwanted elements or to ensure the desired elements are not absorbed by the jarosite structure,[8,10–12] which forms during the hot acid leaching process. The research into AMD has verified the following chemistry of formation for jarosites: hydronium jarosite can only be synthesised under hydrothermal conditions[8,12] and is expected to have a full occupation of H_3O^+/H_2O in the A-site; there is always competition for the A-site between the H_3O^+ and relevant cations in the formation of non-hydronium jarosites, and K is the most favorable cation to fill the A-site;[13] the formation occurs via Fe oxy-hydroxy sulphate complexes stabilized in very low pH solutions and incorporation of a relevant cation causes jarosite precipitation.[8,12]

The approach to the chemistry for researching the magnetic properties of jarosites is in complete contrast to that of AMD. It is essential to try and improve upon the stoichiometry of the jarosite structure in order to be confident that the magnetic properties are not a result of Fe deficiencies: to find high quality models to further the understanding of highly frustrated magnetic systems.[14–18] The antiferromagnetically coupled Fe^{3+} ions make up the best known example of the *kagomé* network; a 2 dimensional lattice of vertex sharing equilateral triangles, an example is shown in Figure 1. Antiferromagnetically coupled ions arranged upon a triangle can not minimise their pairwise interactions and the system becomes highly frustrated resulting in a raised ground state energy. Extending this by tessellating the frustrated plaquettes by edge-sharing, the moments on one triangle dictate the configuration of the neigbouring plaqueettes resulting in the propagation of one coherent ground state through out this lattice. The *kagomé* network is 2 dimensional lattice of vertex sharing triangles and here the moments do not dictate the configuration of neighbouring moments: the geometry of the *kagomé* network prevents a coherent ground state from propagating through out the whole system leading to a macroscopically large degenerate landscape of ground states. In a *kagomé* spin glass it is the random distribution of chiralities and the system traversing all possible ground states through other ground states that gives rise to spin glass like dynamics.[19] What is unique about the *kagomé* spin glass is that all ground states are accessible through all other ground states[20] and it has a T^2 heat capacity[21] as predicted.[19] A T^2 heat capacity is evidence of Goldstone modes, very low energy excitations, present in the system all the way down to 0K.[19] Why the *kagomé* Heisenberg antiferromagnet either displays long range magnetic order [22–25] or a spin glass state[20] rather than remain a spin liquid is due to the presence of anisotropy,[26] either; XY;[19,25] the Dzyaloshinskii-Moriya interaction[27] or Ising[28] and not as a result of Fe vacancies as this paper will demonstrate.

Minimal Fe deficiencies are also necessary to produce a model *kagomé* antiferromagnet to understand the exotic magnetic properties that arise from this highly frustrated manifold. The hydronium end member jarosite is of greatest interest as it undergoes a transition to

an unconventional spin glass state[15, 20] whereas all the other end members undergo long range magnetic order to a Néel state,[22–25] albeit at a reduced temperature virtue of the frustration. Aside from magnetic frustration another component intrinsic to a traditional spin glass is disorder, either site or bond disorder.[29] Randomness introduces further competing interactions between the moments to further prevent a coherent magnetic structure from occurring. Understanding spin glasses are of considerable importance to many subjects. Some high temperature superconductors go through a spin glass phase before the superconducting phase.[30] The out-of-equilibrium dynamics displayed by spin glasses provide important models for systems with similar dynamics such as protein folding[31] and neural networks.[29] The magnetic properties of the jarosites are of fundamental importance for this research; the possibility of a spin glass without intrinsic disorder can be found within hydronium jarosite. Such a proposition will remove averaging from the Hamiltonian which is necessary to take into account a disordered system and instead provide a 'clean' and ordered Hamiltonian[32] that would allow a better explanation of spin glasses and systems displaying out-of-equilibrium dynamics.
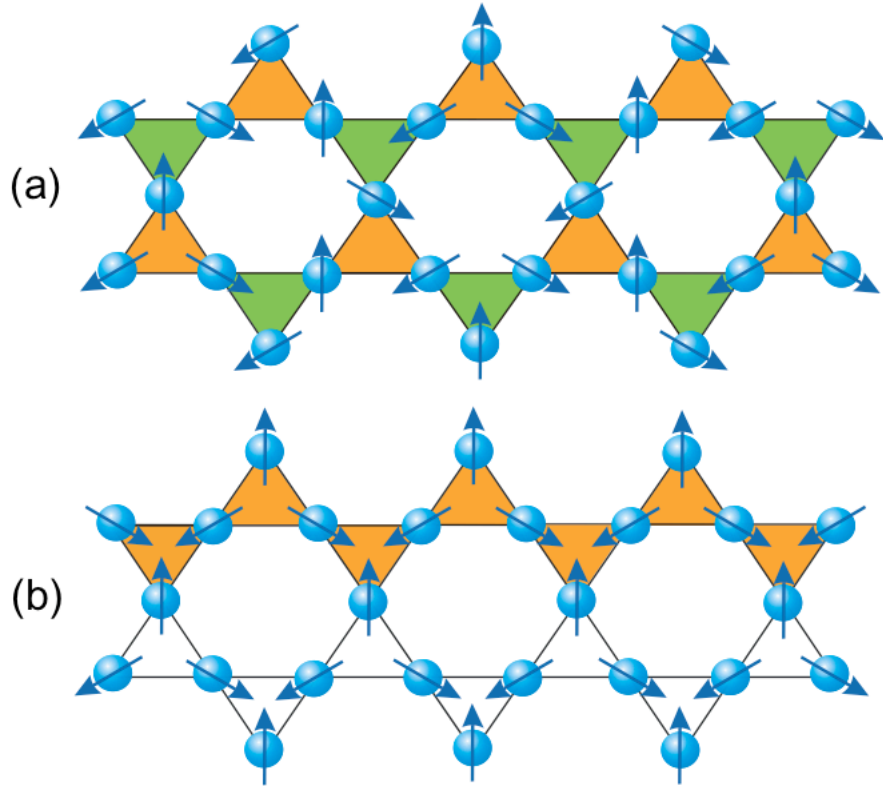

Figure 1: The magnetic frustration of antiferromagnetically coupled ions upon a triangle result in two distinct compromise structures, chiralities, where the neighbouring moments are at 120°. This diagram shows two highly symmetric arrangements of the moments lying in the *kagomé* plane based upon staggered chirality in a) and uniform chiralites in b). The time dependent configurations of a *kagomé* spin glass will evolve through a random distribution of chiralities.

The jarosite crystal structure is best described in the space group $R\bar{3}m$ and has lattice parameters $a \sim 7.3\,\text{Å}$, $c \sim 17\,\text{Å}$. The Fe^{3+}, $S = \frac{5}{2}$, ions make up a series of translationally related *kagomé* layers with an ...ABC... stacking arrangement. These layers are sufficiently well separated that the magnetic Hamiltonian may be considered essentially 2D, R(Fe-Fe)interlayer $\sim 5.64\,\text{Å}$. The Fe-oxygen coordinated octahedra are capped above and below by sulphate tetrahedra groups to form the T-O-T sheets shown in Figure 2a). Separating each of these T-O-T layers is the 12 coordinate site where the A-site ions resides - making the T-A-T sheet (Figure 2a). The magnetic exchange between Fe ions is mediated through the bridging hydroxyl groups, which sit slightly above and below the *kagomé* plane. The *kagomé* network can be seen in Figure 2b and the Fe octahedra are shown in Figure 3 showing the nearest neighbour distance is R(Fe-Fe)intralayer $\sim 3.67\,\text{Å}$. The Fe octahedra is slightly distorted with the apical oxygen slightly further away from Fe center than the equatorial oxygens.

There is a markedly different behaviour between the hydronium and non-hydronium jarosites with all of the non-hydronium iron jarosites ordering at low temperatures into a long-ranged Néel state with the propagation vector k=$(0\ 0\ \frac{3}{2})$, with respect to the hexagonal setting of the space group.[23,24] Whether or not this ordering process is one or two staged appears to depend on the samples.[23,26] In all cases, however, the lower temperature transition occurs at $T_c \sim 55\,\text{K}$.[21,23] Hydronium jarosite, is quite different from the non-hydronium jarosites as it displays a critical spin glass transition at $T_g \sim 17\,\text{K}$..[15,20] In this work our synthesis methods produced samples with a range of spin glass freezing transitions, T_g, between 11 and 20 K.

Elemental analysis is necessary to determine the various factors surrounding the magnetism of the jarosites: why hydronium jarosite only undergoes a spin glass transition whilst all the other jarosite undergo long range order: does this arise because of Fe vacancies or because of the A-site cation?

2 Experimental Section

Many hydronium jarosites were synthesised, in conjunction with several non-hydronium jarosites were made including two K jarosite synthesised by a new oxidative process which claims 100% Fe coverage as well as 100% K in the A-site. For comparison a natural K jarosite from the Margaritas mine, Mexico, provided by Adrian Smith **??** is included in the results.

Hydronium jarosite samples were synthesised from 2g (0.275mol) of $Fe_2(SO_4)_3.5H_2O$ made up to 15cm^3 with either distilled H_2O[15] or $MeOH/H_2O$ mix[14] in a Pyrex pressure tube with a PTFE screw top with a fill ratio of 65% (Ace Glass Inc, screw thread $\sharp$15, 23ml total volume). Phase pure hydronium jarosite crystals suitable for single crystal X-ray diffraction were synthesized at temperatures between 120 and 150°C with a reaction time of 21 hours (variations in time will be indicated for those individual samples). The optimum time for synthesis is a balance between the time needed for crystal growth and the onset of crystal surface dissolution.[33] Earle *et al*[14] claimed that Thermo-gravimetric analyser (TGA) data of the resultant jarosite produced using $MeOH/H_2O$ solvent had a Fe^{3+} vacancy of less than 2%. Our experiments showed that it also enabled control of T_g, in the range 11-20K.

Synthesis conditions for the non-hydronium jarosites prepared under hydrothermal conditions are shown below in Table 1.
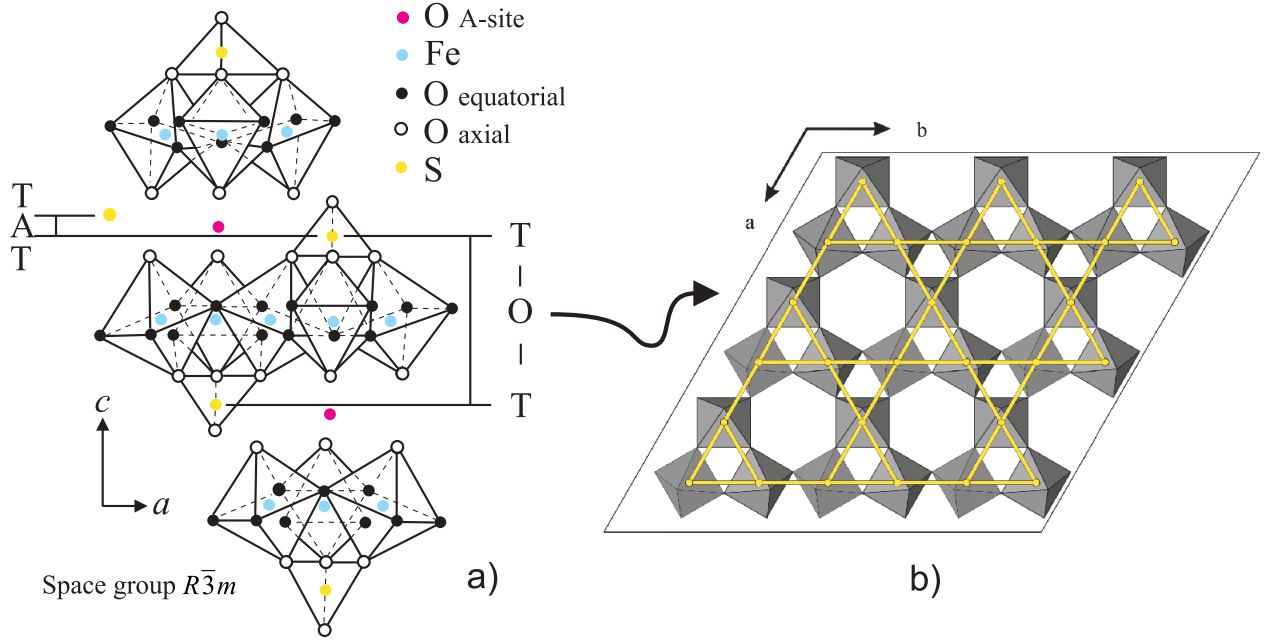
Figure 2: a) Polyhedral representation of hydronium jarosite, the O from the H_3O^+ is shown in red representing the A-site. The bridging hydroxyl groups shown in black, which are just above and below the *kagomé* plane, lead to form a canted Fe-coordinated octahedra. This canting has important consequences for the magnetism of the jarosite structure. b) a view along the c axis showing the canted Fe octahedra and the *kagomé* network overlaid to show the arrangement of the Fe^{3+} ions.
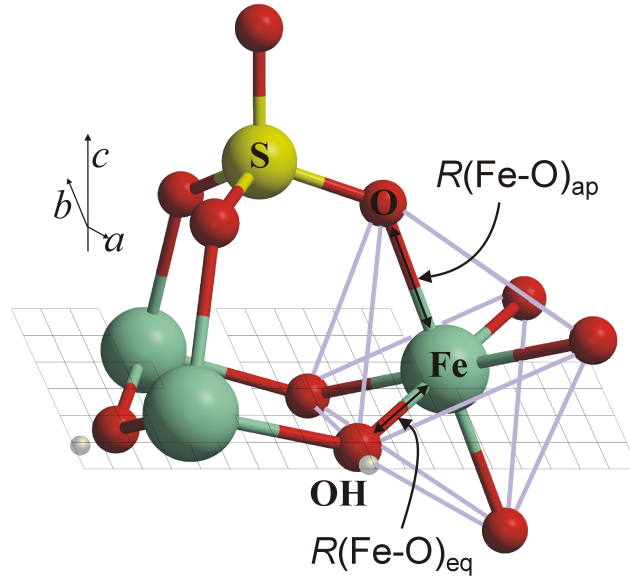

Figure 3: The local coordination of the magnetic Fe^{3+} ions. The apical Fe-O bond is slightly longer than the equatorial Fe-O bond. This distortion may be characterised by the ratio of bond lengths.

5

Table 1: Synthesis conditions for non-hydronium jarosites using Pyrex tubes under hydrothermal conditions all solutions were made up to $15cm^3$ of H_2O.

Sample	A-site SO_4/OH	A^+M	Fe^{3+}M	Temp. (°C)	time (hrs)	yield (g)
KFe1[†]	KOH	0.202	0.55	110	68	1.155
KFe2	K_2SO_4	0.30	0.275	110	48	0.693
KFe3	KOH	0.339	0.55	130	21	1.3342
KFe4	KOH	0.148	0.55	130	21	1.1341
KFe5	K_2SO_4	0.20	0.55	130	21	1.309
KFe6	K_2SO_4	0.046	0.55	130	21	0.905
NaFe1[§]	NaOH	0.33	0.55	130	21	1.186
NaFe2[§]	NaOH	0.12	0.55	130	21	0.926
NaFe3[§]	NaOH	0.90	0.55	130	21	0.724
AgFe1	Ag_2SO_4	0.400	0.55	140	21	1.121
AgFe2[‡]	Ag_2SO_4	0.16	0.55	130	21	1.245
AgFe3	Ag_2SO_4	0.043	0.55	130	21	0.937
RbFe1	Rb_2SO_4	0.42	0.55	130	21	1.1340
RbFe2	Rb_2SO_4	0.25	0.55	130	21	1.0441
RbFe3	Rb_2SO_4	0.039	0.55	130	21	0.7828
NH4Fe1	$(NH_4)_2SO_4$	0.33	0.55	130	21	0.931
NH4Fe2[†]	$(NH_4)_2SO_4$	0.33	0.55	130	21	1.113
NH4Fe3[†]	$(NH_4)_2SO_4$	0.11	0.55	130	21	1.029

[†] pH adjusted with LiOH to bring the starting pH above 1.6
[§] Sodium jarosite could only be successfully synthesised using NaOH
[‡] Contains impurities, Ag_2SO_4 and Ag

The non-hydronium jarosites were synthesised using new redox methods[34] where iron wire is oxidized.[18] This improves upon Fe coverage and also produced significantly larger single crystals $\geq 50\mu$m. The following $Na_2(SO_4)_2$ (0.85g, 0.12mol (lower concentration required for Na)), $K_2(SO_4)_2$ (2.44g, 0.28mol), $Ag_2(SO_4)_2$ (4.37g, 0.28mol), $Rb_2(SO_4)_2$ (3.74g, 0.28mol) and $(NH_4)_2(SO_4)_2$ (1.85g, 0.28mol) were each dissolved and made up to $25cm^3$ with distilled water, to which $1.1cm^3$ of concentrated H_2SO_4 was added. For each reaction 0.336g of iron wire, 2mm diameter, 99.9%, was cut into 4-5 smaller pieces and put along with the relevant A-site sulfate solution into a pressure tube ($38cm^3$ total capacity). The reaction took place at 170°C over 48 hours and is heavily dependent upon oxygen partial pressure.

In comparison with K-Jarosite, formation of the other A-site jarosites was more difficult, often producing hematite or mixed phase of hematite and jarosite.

Elemental analysis was carried out using Inductively Coupled Plasma - Optical Emission Spectra (ICP-OES), a wet chemistry technique that measures the intensity of emission spectra from ionised elements, heated in an argon torch. The machine used was a Perkin-Elmer Optima 3300RL ICP-OES operating at 1.5 cm^3 per minute. The samples are mounted on a AS91 autosampler and solution is drawn up through each position on the autosampler using a peristaltic pump into the cross-flow type nebulizer and from there the sample is sprayed

into a Ar plasma torch. The resultant spectral emission lines are separated by an Echelle grating polychromator and detected using segmented-array charge-coupled-device detector. ICP-OES operating settings were: frequency 40Hz; power 1.3kW and observation height of 15mm. All samples were weighed out at 0.1000g±0.0002g and were dissolved in 2cm^3 of HCL/HNO$_3$ and were gently warmed until dissolved. A further 18cm^3 of distilled water was added after to make up the solution to 20cm^3. sample KFeMIT was limited in mass and only 0.0300g±0.0002g were dissolved and made up to a solution of 20cm^3.

The data was analysed by initially working out which spectral wavelength (channel) for each element produced the smallest standard deviation in intensities with reference to the periodic arranged of blanks on the autosampler. The intensities of a chosen channel from each sample had to be corrected for drift. This was done by a linear interpolation of the drift of each of the sample intensities between the periodic arrangement of the blanks. A calibration curve was set up by obtaining the gradient of the chosen channel from the intensities of known standard ppm element solutions also arranged upon the autosample. For sulphur, 10ppm and 1000pm standard solutions were used and for Fe 10ppm, 500ppm and 1000ppm standard solutions were used. The Fe calibration curve was extrapolated as the Fe intensity from the samples was approxiamtely twice that for Fe 1000ppm. This is a reasonable approach as chamber saturation approaches 3 million counts, our data produced in the region of 1500 counts for Fe. The Perkin-Elmer Optima 3300RL instrument is stated to have an uncertainty of 0.13% for Fe but no data is available for S. Also due to oxygen (from air) present in the chamber, sulphur counts were lower at approximately 600 counts. Sulphur precision was obtained from actual experimental standard deviations generated from the periodic arrangement of blanks and sulphur 10ppm standards placed at intervals no greater than 1 between every 10 samples on the autosampler. This generated a good experimental error which showed that the sulphur counts for 10ppm were consistent and the experimental standard deviation produced an overall error of ±0.93% for Fe coverage. Once the calibration curve is known then the concentrations in ppm can be calculated and the corresponding relative molar quantities for each sample. Conversion is simple; divide the concentrations in ppm through by the relative atomic mass for Fe or S. The relative formula amount of Fe is obtained by dividing the Fe mmol quantity through by the S mmol value and multiplying by 2. The rules for determining jarosite stoichiometric formula are laid out by Kubisz,[12] and that states that the sulphate value is always 2 and the formula is obtained relative to the sulphate group. Likewise the A-site occupation was worked out in the same manner, relative to the sulphate group.

Magnetic measurements were performed on a Quantum Design superconducting quantum interference device magnetometer (SQUID) - MPMS-7. The magnetic measurements shown in this work were obtained from zero field cooled/field cooled meaurements (ZFC/FC). All hydronium jarosite samples and most non-hydronium samples were cooled down to the lowest temperature possible, $2\,\mathrm{K}$ – otherwise, $5\,\mathrm{K}$, in zero applied field, from a temperature far above the expected transitions temperatures ($T_\mathrm{g} \sim 11 - 20\,\mathrm{K}$ for hydronium jarosite and $45 - 65\,\mathrm{K}$ for non-hydronium jarosites). At base temperature and after waiting for the sample to reach thermal equilibrium an external field of $100\,\mathrm{Oe}$ was applied for all jarosites, unless specified. The sample is warmed and throughout the magnetic moment is measured at various temperatures according to a predetermined sequence. Measurements are usually taken at temperature steps of $0.5\,\mathrm{K}$ or $0.25\,\mathrm{K}$ through the transition region; whereas larger steps, 10-

20 K, are sufficient for Curie-Wiess determination in the paramagnetic temperature region. After the final measurement the sample is cooled back down to the base temperature with the same applied field. After thermal equilibrium has been reached the sequence of measurements is repeated. The spin glass freezing transition was determined from the discontinuity in the field cooled data set. The corresponding error was ± 0.2 K.

Powder diffraction data collected to confirm phase purity was collected on an X'Pert Pro diffractometer with X'Celerator PSD detector. Data was collected between $8° - 143°\,(2\theta)$ with a step size of $0.07°$ using a Co source with a Ge 111 primary monochromator (1.78901 Å). The sample was prepared by backfilling onto a sample mount and the data was collected in Bragg-Bretano geometry.

3   Results

The ICP-OES results laid out below are kept generally in sequence order on the autosampler. Tables 2, 3, 4 and 5 present the ICP-OES data. They are grouped as hydronium and non-hydronium jarosites. The formulas quoted in Table 5 are based upon the 500ppm calibration curve instead to make a comparison for all the non-hydronium iron jarosites with sample KFeRedox (Table 5). The Fe concentration of KFeRedox lies within the Fe 500ppm calibration range and in consideration that the oxidative method purports 100% Fe coverage,[18] this is the best method of comparison with the other non-hydronium samples.

The introduction of known non-jarosite samples, *e.g.* H3OS20 (Table 2), H3OS29 and H3OS38 (Table 3) shows that the technique is viable and that an expected null result is obtained. It appears that MeOH concentration has more effect on the Fe coverage rather than temperature as can be seen that low MeOH concentration coincides with high Fe coverage for all temperatures. This result extends for Table 3. The very high MeOH concentrations result in unwanted Fe oxy-hydroxy sulphates; at the modest temperature of $120°$C it promotes the growth of X-ray diffraction amorphous Schwertmannite 4(c) and at higher temperatures gives rise to other unwanted Fe oxy-hydroxy sulphates, H3OS36 and H3OS37 (Table 3) which all give substantially lower values for Fe coverage. An assumption can be made from Figure 7(a) that lower values of T_g coincide with lower Fe coverage. Plotting of this data in Figure 7(a) shows a slight trend with T_g and Fe coverage, though the fit is poor (R=0.7034) and does not suggest that this is the factor which alters or determines the onset of a spin glass transition and or why the non-hydronium jarosites (ICP-OES results shown in Table 5) which have similar or poorer Fe coverage still undergo long range magnetic order.

Similarly, the Fe occupation is high, or can be taken to be very high, for all of the hydronium jarosite samples, though unsubstantiated drift might be occurring towards the end of the measurements for the hydronium samples in Table 4 prepared using 100% H_2O as solvent. It appears neither the time nor temperature of synthesis have a well defined impact upon Fe coverage. Likewise, looking at the values of T_g, there is no apparent correlation between these and the Fe coverage for hydronium jarosite samples prepared using 100% H_2O as solvent, though the range in T_g is smaller compared to hydronium jarosites prepared using MeOH/H_2O mixes. Figure 7(b) is in addition to Figure 7(a) showing the all hydronium jarosites with T_g plotted against Fe % coverage, it confirms that although lower values of T_g can be achieved using high concentrations of MeOH and that there is a corresponding

| Sample	Temp(°C)	%H_2O	Fe (mmol)	SO_4 (mmol)	Fe:SO_4	Formula	T_g (K) ± 0.2K
H3OFeS1	150	90	27.198	18.014	3.02	$H_3OFe_{3.00}(SO_4)_2(OH)_{6.00}$	15.71
H3OFeS2	150	80	27.153	18.209	2.98	$H_3OFe_{2.98}(SO_4)_2(OH)_{5.95}(H_2O)_{0.05}$	15.36
H3OFeS3	150	70	26.704	18.248	2.93	$H_3OFe_{2.93}(SO_4)_2(OH)_{5.78}(H_2O)_{0.22}$	14.76
H3OFeS4	150	60	28.090	19.040	2.95	$H_3OFe_{2.95}(SO_4)_2(OH)_{5.85}(H_2O)_{0.15}$	13.87
H3OFeS9	120	90	27.640	18.828	2.94	$H_3OFe_{2.94}(SO_4)_2(OH)_{5.81}(H_2O)_{0.19}$	18.80
H3OFeS10	120	80	28.389	18.879	3.01	$H_3OFe_{3.00}(SO_4)_2(OH)_{6.00}$	18.38
H3OFeS11	120	70	28.925	19.397	2.98	$H_3OFe_{2.98}(SO_4)_2(OH)_{5.95}(H_2O)_{0.05}$	17.28
H3OFeS13	120	50	28.220	19.559	2.89	$H_3OFe_{2.89}(SO_4)_2(OH)_{5.66}(H_2O)_{0.34}$	14.84
H3OFeS14	120	40	28.099	19.724	2.85	$H_3OFe_{2.85}(SO_4)_2(OH)_{5.55}(H_2O)_{0.45}$	12.73
H3OFeS15	120	30	27.100	19.655	2.76	$H_3OFe_{2.76}(SO_4)_2(OH)_{5.27}(H_2O)_{0.73}$	11.84
H3OFeS16§	120	20	26.676	21.311	2.50	$H_3OFe_{2.50}(SO_4)_2(OH)_{4.51}(H_2O)_{1.49}$	11.26
H3OFeS17	150	75	27.555	18.824	2.93	$H_3OFe_{2.93}(SO_4)_2(OH)_{5.78}(H_2O)_{0.22}$	14.63
H3OFeS18	150	65	27.993	19.172	2.92	$H_3OFe_{2.92}(SO_4)_2(OH)_{5.76}(H_2O)_{0.24}$	14.50
H3OFeS20†	120	10	23.908	24.697	1.94	$H_3OFe_{1.94}(SO_4)_2(OH)_{2.81}(H_2O)_{3.19}$	N/A

§ The appearance of Schwertmannite as evidenced under SEM Figure 4(c)

† Possible Mikasaite - crystalline $Fe_2(SO_4)_3$ - evidenced from SEM Figure 4(d)
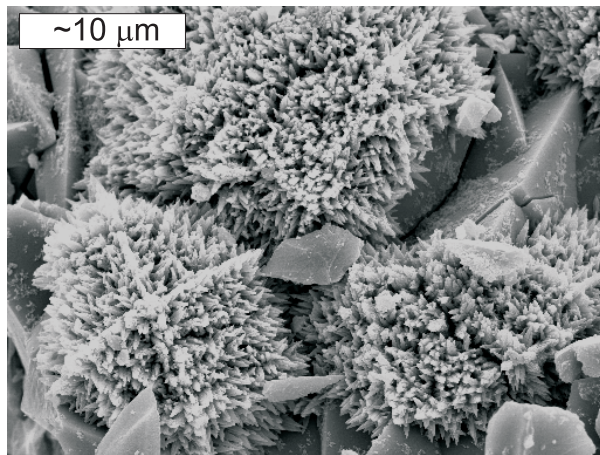
Table 2: Elemental analysis results of MeOH solvent prepared hydronium jarosites using a Perkin-Elmer Optima 3300RL ICP-OES. The results are displayed in order of the experimental sequence.
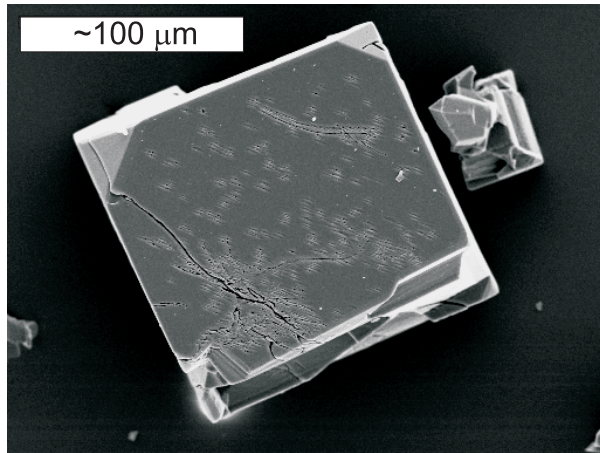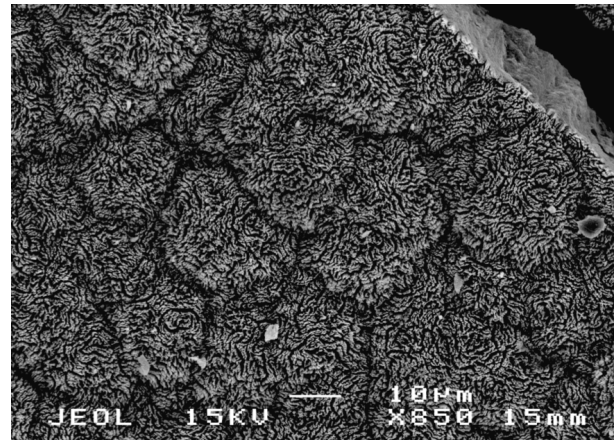
(a) 100% H_2O 150°C 21 hours
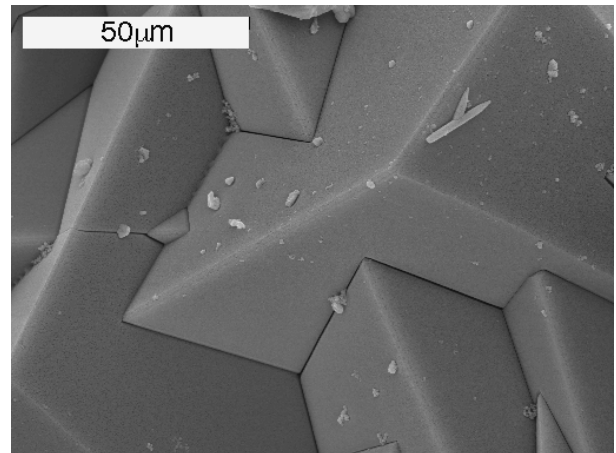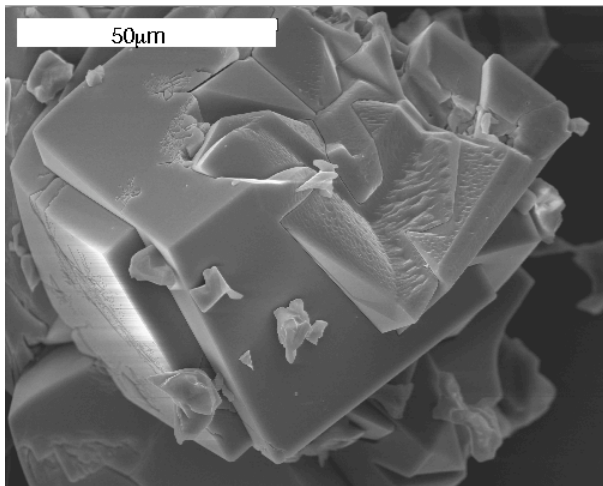
(b) 40:60 MeOH:H_2O 120°C 21 hours

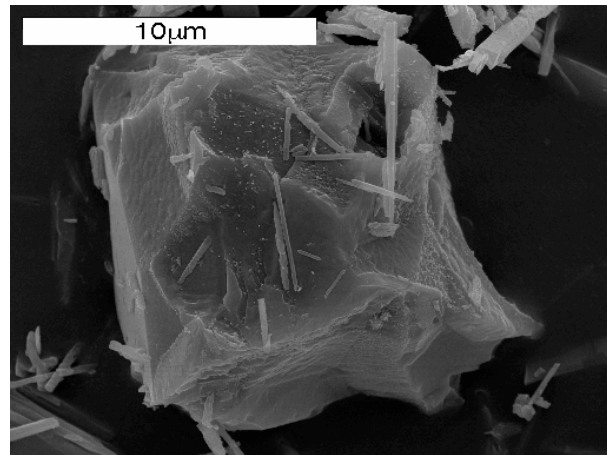(c) 80:20 MeOH:H_2O 120°C 21 hours

(d) 90:10 MeOH:H_2O 120°C 21 hours - mikasaite

Figure 4: SEM images (b), (c) and (d) are the product from various H_2O/MeOH mixeses at various temperatures and (a) is produced from 100% H_2O as the solvent at 150°C. (a) is a large single crystal of hydronium jarosite with a pseudo cubic morphology, however, the distortion from ideal pseudo cubic morphology occurs with increasing MeOH concentration in the solvent and in combination with high temperatures. (b) is an example of jarosite formed in high MeOH concentration with modest temperatures causing the morphology to change to triangular prisms. Very high concentrations at modest temperatures produce unwanted Fe oxy-hydroxy sulpahtes as shown by the occurrence of Schwertmannite (corel-like appearance) in (c) and eventually leading to Mikasaite, (d), produced from the maximum concentration of MeOH solvent. The formation of Mikasaite - crystalline Fe_2SO_4 - is not necessarily an end product but the formation of a precursor to hydronium jarosite precipitation at which point the reaction ceases to continue in these extreme conditions.

(a) 40:60 MeOH:H_2O 130°C 21 hours

(b) 60:40 MeOH:H_2O 150°C 21 hours
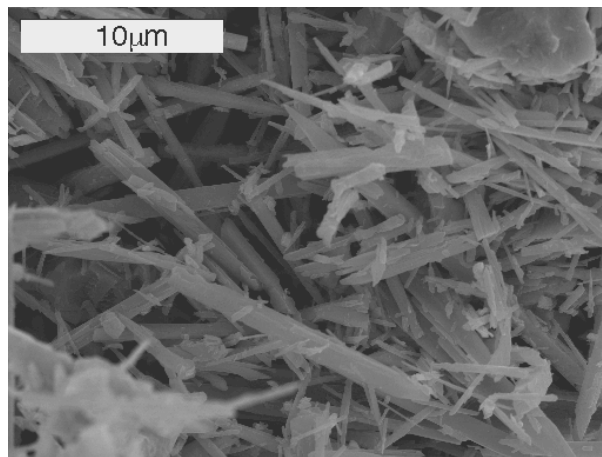
(c) 60:40 MeOH:H_2O 150°C 21 hours

Figure 5: SEM images (a), (b) and (c) are the product from various H_2O/MeOH mixeses at various temperatures. Instead of a morphology change from pseudo cubic to triangular prisms as shown in Figure 4(b), pseudo cubes still form, but the effect of stripping the A-site[33] is increased in the presence of MeOH as shown in (a). Increasing temperature and MeOH results in severely mottled pseudo cubes, (b), and produce needle shaped structures of unwanted Fe oxy-hydroxy sulphates, (c).

Sample	Temp(°C)	%H_2O	Fe (mmol)	SO_4 (mmol)	Fe:SO_4	Formula	T_g (K) ±0.2K
H3OFeS21	130	90	28.349	18.937	2.99	$H_3OFe_{2.99}(SO_4)_2(OH)_{5.98}(H_2O)_{0.02}$	17.36
H3OFeS22	130	80	28.396	19.354	2.93	$H_3OFe_{2.93}(SO_4)_2(OH)_{5.80}(H_2O)_{0.20}$	16.52
H3OFeS23	130	70	28.260	19.133	2.95	$H_3OFe_{2.95}(SO_4)_2(OH)_{5.86}(H_2O)_{0.14}$	12.02
H3OFeS24	130	60	27.453	18.778	2.92	$H_3OFe_{2.92}(SO_4)_2(OH)_{5.77}(H_2O)_{0.23}$	13.65
H3OFeS26	130	50	27.493	19.063	2.88	$H_3OFe_{2.88}(SO_4)_2(OH)_{5.65}(H_2O)_{0.35}$	12.00
H3OFeS27	130	40	27.066	19.501	2.78	$H_3OFe_{2.78}(SO_4)_2(OH)_{5.33}(H_2O)_{0.67}$	11.57
H3OFeS28	130	30	26.713	19.826	2.69	$H_3OFe_{2.69}(SO_4)_2(OH)_{5.08}(H_2O)_{0.92}$	10.92
H3OFeS29[†]	130	20	22.844	24.153	1.89	$H_3OFe_{1.89}(SO_4)_2(OH)_{2.67}(H_2O)_{3.33}$	N/A
H3OFeS30	140	90	27.518	19.287	2.85	$H_3OFe_{2.85}(SO_4)_2(OH)_{5.56}(H_2O)_{0.44}$	14.17
H3OFeS31	140	80	27.892	19.680	2.83	$H_3OFe_{2.83}(SO_4)_2(OH)_{5.50}(H_2O)_{0.50}$	15.10
H3OFeS32	140	70	27.300	19.668	2.78	$H_3OFe_{2.78}(SO_4)_2(OH)_{5.33}(H_2O)_{0.67}$	14.38
H3OFeS33	140	60	27.672	19.577	2.83	$H_3OFe_{2.83}(SO_4)_2(OH)_{5.48}(H_2O)_{0.52}$	13.70
H3OFeS34	140	50	27.901	19.966	2.79	$H_3OFe_{2.79}(SO_4)_2(OH)_{5.38}(H_2O)_{0.62}$	13.85
H3OFeS35[‡]	140	40	27.756	20.345	2.73	$H_3OFe_{2.73}(SO_4)_2(OH)_{5.19}(H_2O)_{0.81}$	12.34
H3OFeS36[‡]	140	30	27.363	21.980	2.49	$H_3OFe_{2.49}(SO_4)_2(OH)_{4.47}(H_2O)_{1.53}$	11.53
H3OFeS37[‡]	140	20	26.515	24.139	2.20	$H_3OFe_{2.20}(SO_4)_2(OH)_{3.59}(H_2O)_{2.41}$	10.92
H3OFeS38[†]	140	10	26.044	27.209	1.91	$H_3OFe_{1.91}(SO_4)_2(OH)_{2.74}(H_2O)_{3.26}$	N/A

[†] Possible Mikasaite - crystalline $Fe_2(SO_4)_3$ similar product produced as for sample H3OS20 refer to SEM Figure 4(d)

[‡] Contains another phase of unwanted Fe oxy-hydroxy sulphates determined from powder XRD

Table 3: Elemental analysis results of MeOH solvent prepared hydronium jarosites using Perkin-Elmer Optima 3300RL ICP-OES. The results are displayed in order of the experimental sequence.

Sample	Temp(°C)	Time (hrs)	Fe (mmol)	SO$_4$ (mmol)	Fe:SO$_4$	Formula	T_g (K) $\pm$0.2K
H3OFe021	150	15	29.542	31.932	2.97	H$_3$OFe$_{2.97}$(SO$_4$)$_2$(OH)$_{5.90}$(H$_2$O)$_{0.10}$	15.80
H3OFe021	150	15	29.577	31.970	2.97	H$_3$OFe$_{2.97}$(SO$_4$)$_2$(OH)$_{5.90}$(H$_2$O)$_{0.10}$	15.80
H30Fe022	145	21	29.937	32.359	3.04	H$_3$OFe$_{3.00}$(SO$_4$)$_2$(OH)$_{6.00}$	14.67
H3OFe023	150	80	29.209	31.571	3.05	H$_3$OFe$_{3.00}$(SO$_4$)$_2$(OH)$_{6.00}$	15.71
H3OFe023	150	80	30.067	32.491	3.06	H$_3$OFe$_{3.00}$(SO$_4$)$_2$(OH)$_{6.00}$	15.71
H30Fe024	150	21	29.989	32.415	3.04	H$_3$OFe$_{3.00}$(SO$_4$)$_2$(OH)$_{6.00}$	15.69
H3OFe047	142	21	30.342	32.796	3.09	H$_3$OFe$_{3.00}$(SO$_4$)$_2$(OH)$_{6.00}$	16.80
H3OFe048	138	21	30.078	32.511	3.09	H$_3$OFe$_{3.00}$(SO$_4$)$_2$(OH)$_{6.00}$	16.64
H3OFe049	145	21	29.580	31.972	3.04	H$_3$OFe$_{3.00}$(SO$_4$)$_2$(OH)$_{6.00}$	15.80
H3OFe050	142	21	29.558	31.949	3.11	H$_3$OFe$_{3.00}$(SO$_4$)$_2$(OH)$_{6.00}$	17.21
H3OFe051	150	4	28.979	31.323	3.06	H$_3$OFe$_{3.00}$(SO$_4$)$_2$(OH)$_{6.00}$	15.52
H3OFe052	138	21	29.129	31.485	3.15	H$_3$OFe$_{3.00}$(SO$_4$)$_2$(OH)$_{6.00}$	17.50

Table 4: Elemental analysis results of 100%H$_2$O solvent prepared hydronium jarosites using a Perkin-Elmer Optima 3300RL ICP-OES. The results are displayed in order of the experimental sequence.

decrease in Fe coverage, only 1 sample in the 41 listed hydronium samples used for this ICP-OES analysis has a Fe coverage less than 90%. Higher concentrations of methanol result in changes to the morphology leading to triangular prisms as shown in Figure 4(b). This appears to be a stability limit: if the Fe coverage is any lower, the sample is no longer homogeneous hydronium jarosite or hydronium jarosite: this can be seen in samples H3OS16, H3OS20, H3OS29, H3OS36-H3OS38 where unwanted Fe oxy-hydroxy sulphates appear, refer to SEM Figures 4(c) and 4(d). This is contrasted with the large pseudo cubes of hydronium jarosite prepared using 100% H_2O in Figure 4(a).

X-ray powder diffraction data of the following samples H3OFeS34, H3OFeS35 and H3OS36 (Figure 6), also confirms the presence of an unwanted Fe oxy-hydroxy sulphates with the appearance of two reflections from samples H3OFeS35 and H3OFeS36 and a weak third peak from sample H3OFeS36, all at slightly lower 2θ values than the two jarosite reflections as shown in the insert of Figure 6. The jarosite peak positions were generated from a known structural model[15] and the unwanted phases were determined by pattern matching using the software Eva, by Bruker. Eva contains a database under license from the International Centre for Diffraction Data (ICDD) and the software determined an unwanted Fe oxy-hydroxy sulphate phase to be Fe sulphate hydroxide - $2Fe(OH)SO_4/Fe_2O_3.2SO_3.H_2O$, ICDD reference 21:0428; no further crystallographic details could be obtained. The overall diffraction patterns for samples H3OFeS35 and H3OFeS36 may show the appearance of other Fe sulpates hydrates/hydroxides. The small presence of other unwanted Fe oxy-hydroxy sulphates may explain the reduction of the Fe occupation: Kubisz rules[12] will no longer hold with an increase in other unwanted Fe oxy-hydroxy sulphates which typically have a lower Fe % weight than hydronium jarosite according to the other possible Fe oxy-hydroxy phases determined by Eva. This may explain the drop in Fe coverage between sample H3OFeS34 (93%) and H3OFeS37 (73%). High Fe coverage is crucial for the formation of hydronium jarosite and is unlikely to determine the nature and temperature of the spin glass transition. Consequently another factor must an energy scale, that determines the spin glass transition in the hydronium jarosites and distinguishes it from non-hydronium jarosites. Table 5 demonstrates that Fe coverage is not responsible for the nature and the temperature of the magnetic transition for the non-hydronium jarosites.

The non-hydronium jarosites provide a very interesting contrast to the hydronium jarosites: firstly that even lower Fe coverage can be sustained still retaining the jarosite structure. This is evident with the synthetic potassium jarosite formed under forced hydrolysis conditions, samples KFe1, KFe3-6 all have low Fe coverage reaching as little as 81%. This was also noted in previous work[6] where potassium jarosites made in non-hydrothermal conditions ($\sim 98°C$) have a similar Fe coverage $\sim 82\%$. This Fe loss is incredible as it corresponds to a fifth of all Fe atoms, and yet long range magnetic order still persists with similar transition temperatures for KFeRedox which has a Fe coverage of $\sim 100\%$. This then proves that any disorder from Fe vacancy has minimal effect upon the magnetism which confers with recent reported work[35] It has been calculated that the percolation limit for the *kagomé* network using nearest neighbour interactions (Potts model with q=1) is either for bond or site disorder are 0.524^{36} and 0.653^{37} respectively, thus confirming if the structure can withstand further defects before collapse, long range magnetic order might still be expected. Other work looking into site vacancies have shown through computer simulations that there is an energy barrier to the formation of Fe vancancies and are unlikely to form.[38] A recent retrospective review
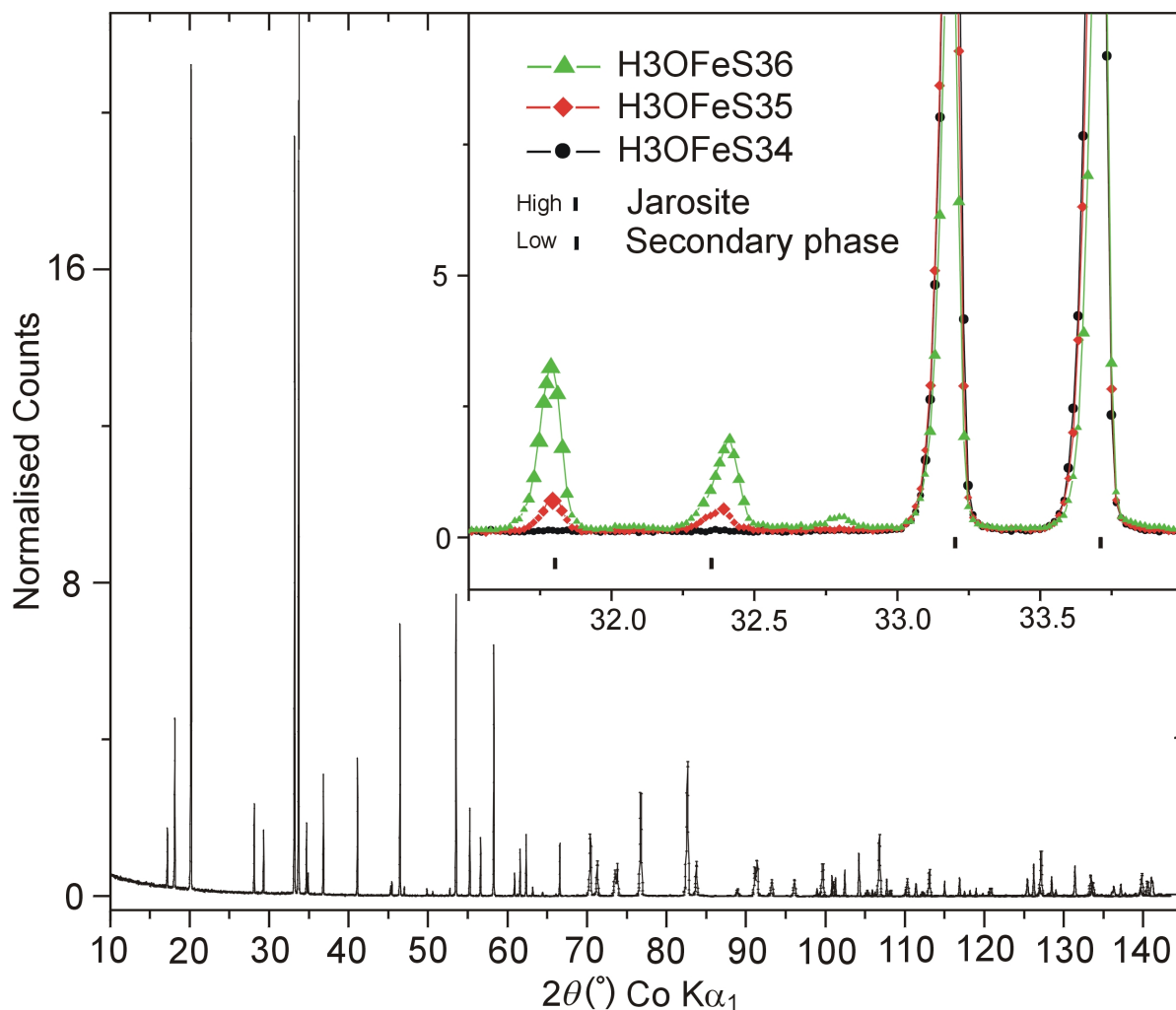
Figure 6: shows a diffraction for sample H3OFeS34, the data was collected on a Pananalytical X'pert Pro with a Co source and Ge111 monochromator. The figure insert shows that sample H3OFeS34 (black circles) has no impurity phase, whereas samples H3OFeS35 (red diamonds) and H3OFeS36 (green triangles) clearly show an unwanted secondary phase present. The occurrence of an impurity phase is concomitant with very high concentrations of MeOH and subsequent deterioration in the pseudo cubic morphology (Figures 4 and 5) and fall in Fe coverage (Table 3). The secondary phase was determined from the pattern matching software Eva and is likely to be a phase of iron sulphate hydroxide (ICDD ref: 21:0428).

Sample	A-site (mmol)	Fe (mmol)	SO_4 (mmol)	Fe:SO_4[§]	Formula[‡]	T_c (K) ±0.2K
RbFe1		23.451	16.675	2.81	$RbFe_{2.81}(SO_4)_2(OH)_{5.44}(H_2O)_{0.56}$	63.85, (50.00)
RbFe2		23.736	16.344	2.91	$RbFe_{2.91}(SO_4)_2(OH)_{5.71}(H_2O)_{0.29}$	64.20, 50.65
RbFe3		23.413	16.871	2.78	$RbFe_{2.78}(SO_4)_2(OH)_{5.33}(H_2O)_{0.67}$	45.00
NaFe1	7.227	25.281	18.395	2.75	$Na_{0.79}(H_3O)_{0.21}Fe_{2.75}(SO_4)_2(OH)_{5.25}(H_2O)_{0.75}$	(60.75), 43.90
NaFe2	5.295	26.972	18.980	2.84	$Na_{0.56}(H_3O)_{0.44}Fe_{2.84}(SO_4)_2(OH)_{5.53}(H_2O)_{0.47}$	(61.00), 43.00
NaFe3	3.882	26.766	19.091	2.80	$Na_{0.41}(H_3O)_{0.59}Fe_{2.80}(SO_4)_2(OH)_{5.41}(H_2O)_{0.59}$	(60.00), 39.50
NH4Fe1		25.586	18.822	2.72	$NH_4Fe_{2.72}(SO_4)_2(OH)_{5.16}(H_2O)_{0.84}$	61.35, 52.05
NH4Fe2		26.543	18.729	2.83	$NH_4Fe_{2.83}(SO_4)_2(OH)_{5.50}(H_2O)_{0.50}$	43.50
NH4Fe3		26.807	19.128	2.80	$NH_4Fe_{2.80}(SO_4)_2(OH)_{5.41}(H_2O)_{0.59}$	61.25, 50.50
KFe1	8.485	25.205	19.202	2.63	$K_{0.88}(H_3O)_{0.12}Fe_{2.63}(SO_4)_2(OH)_{4.88}(H_2O)_{0.10}$	45.00, 64.50
KFe3	8.566	24.580	18.819	2.61	$K_{0.91}(H_3O)_{0.09}Fe_{2.61}(SO_4)_2(OH)_{4.84}(H_2O)_{0.10}$	64.24
KFe4	7.975	25.367	19.397	2.62	$K_{0.82}(H_3O)_{0.18}Fe_{2.62}(SO_4)_2(OH)_{4.85}(H_2O)_{0.10}$	(64.20), 50.30
KFe5	8.163	24.346	19.954	2.44	$K_{0.82}(H_3O)_{0.18}Fe_{2.44}(SO_4)_2(OH)_{4.32}(H_2O)_{0.10}$	63.55, 47.00
KFe6	7.042	25.029	19.873	2.53	$K_{0.71}(H_3O)_{0.29}Fe_{2.53}(SO_4)_2(OH)_{4.56}(H_2O)_{0.10}$	47.30
KFeRedox[†]	2.589	7.469	4.975	3.00	$KFe_{3.00}(SO_4)_2(OH)_6$	65.00
KFe$_{natural}$[*]				2.99	$KFe_{2.99}(SO_4)_2(OH)_{5.97}(H_2O)_{0.03}$	63.20, 50.55
KFeRedox_11		33.27[‡]		2.98	$KFe_{2.98}(SO_4)_2(OH)_{5.94}(H_2O)_{0.06}$	62.50, 53.58
AgFe1		20.707	15.400	2.69	$AgFe_{2.69}(SO_4)_2(OH)_{5.07}(H_2O)_{0.93}$	N/A
AgFe2		22.643	16.578	2.73	$AgFe_{2.73}(SO_4)_2(OH)_{5.12}(H_2O)_{0.80}$	N/A
AgFe3		22.515	16.791	2.68	$AgFe_{2.68}(SO_4)_2(OH)_{5.05}(H_2O)_{0.95}$	44.30

[§] The Fe:S ratio was produced using the calibration curve between Fe 10ppm and 500ppm to make a comparison with KeRedox, which further verifies that the oxidatative preparation produces 100% Fe coverage.[18]

[‡] A-site determination can not be carried out for the elements Ag, Rb and NH_4 with this technique.

[†] The χ was measured in a field of 1000G due to small sample mass. The higher applied field strength might have suppressed the response from a second transition.

[*] Elemental analysis by electron microscopy[6]

[‡] Actual % weight value for Fe. Measurement taken on the same machine with a different calibration method.

Table 5: Elemental analysis results for non-H_3O^+ jarosites using a Perkin-Elmer Optima 3300RL ICP-OES. The results are displayed in order of the experimental sequence. by the A-site. Increase in the the uptake of hydronium in the A-site results in a decrease in temperature for the magnetic transitions. The non-hydronium jarosites generally show two transitions, labeled T_{N_1} and T_{N_2}: T_{N_1} occurs higher in temperature.

on SCGO[39] - another structure containing a *kagomé* network made up from Cr^{3+} ions show similarly the magnetic system (short range magnetic correlations to 0K) is robust to site vacancies of Cr^{3+} ions.[40]

Another important aspect of the data shown in Table 5 is that the concentrations of A-site used has little effect on the Fe coverage, but does correlate with A-site uptake versus hydronium uptake; apart from the potassium jarosite where K uptake is far more preferable to hydronium uptake. These results confirm the formation mechanism for jarosites as explained earlier, that the jarosite precursor is not determined by the A-site. Increase in the the uptake of hydronium in the A-site results in a decrease in temperature for the magnetic transitions and this is reported in recent work.[35] The non-hydronium jarosites generally show two transitions, labeled T_{N_1} and T_{N_2}. Transition T_{N_1} occurs higher in temperature (60-65K) and T_{N_2} appears lower (45-55K). Increase of hydronium in the A-site results in T_{N_1} becoming broader and eventually no longer discernible from the susceptibility data. Values of T_{N_1} that are broad are shown in parentheses in Table 5. Relative high occupations of hydronium in the A-site will also decrease the temperature at which the final (only) transition occurs, this can be seen by referring to Table 5, examples of samples with a high hydronium content (refer to Table 1 for synthesis conditions) and correspondingly low single magnetic transitions are RbFe3, NaFe3, NH4Fe3, KFe6 and AgFe3.

4 Conclusion

The ICP-OES results show some very important points in connection with the magnetism and the structure of the jarosite mineral. Firstly, that the hydronium jarosite structure has less tolerance to Fe disorder than the non-hydronium analogues, a possible explanation for hydronium jarosite being prone to stacking faults[41] as highlighted in Figure 8.

Further, it has been shown, that increase in MeOH concentration for the solvent leads to a decrease in T_g, though not necessarily closely related to Fe coverage as shown in Figure 7. The same figure indicates that very low values of T_g correspond to defects in Fe coverage, but more likely that the Fe deficiency coincides with the breakdown of the hydronium jarosite structure into other unwanted Fe-oxy-hydroxy sulphates and it is a structural change that drives the magnetic transition. Susceptibility data for samples with very low values of T_g have a large super-paramagnetic-like background below T_g. Whether this comes from non-jarosite phases of Fe oxy-hydroxy sulphates or from the jarosite sample itself is not clear, especially when secondary phases are not observed through SEM or powder XRD. If it can be shown that the presence of unwanted Fe oxy-hydroxy sulphates do not affect the bulk magnetic response, an increase in super-paramagnetic contributions may point towards the occurrence of solitons[42] in the *kagomé* spin glass state as moments decouple from the frustrated manifold and propagate as free spins. Such solitons would be present in the spin glass phase and above close to T_g, when the spins form a spin liquid phase. Figures 9 and 10 highlight the presence of increasing super-paramagnetic background with increasing values of χ with decreasing values of T_g. What is also observed is smearing of the spin glass freezing transition with decreasing T_g. It is clear from the elemental analysis of the hydronium jarosites is that a variation of values for T_g can occur with minimal Fe loss and that equally high Fe coverage is obtained through synthesis with $MeOH/H_2O$ solvent as well as 100% H_2O solvent. There
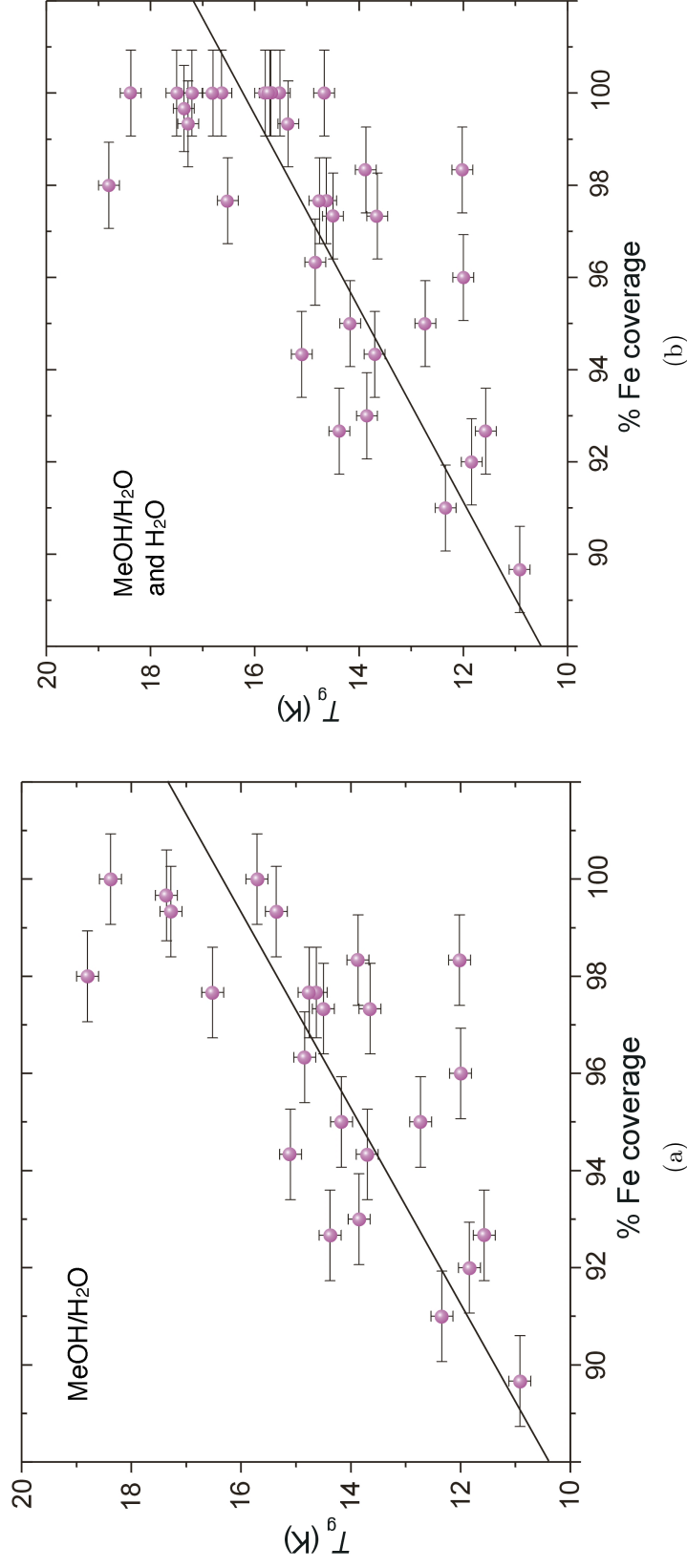
Figure 7: (a) is a plot of T_g against Fe coverage for hydronium samples prepared using MeOH as part of the solvent and (b) is a plot of T_g against Fe coverage for all hydronium samples used for in the ICP-OES analysis. The graphs show that the lowest spin glass freezing temperatures are obtained with higher concentrations of the MeOH and corresponds to a slight decrease in Fe % coverage. The data in the graphs show there is no clear relation between Fe coverage and T_g. It is noted that the hydronium jarosites prepared in 100% H_2O solvent appear to have near perfect 100% Fe coverage and still possess a significant variation in T_g.
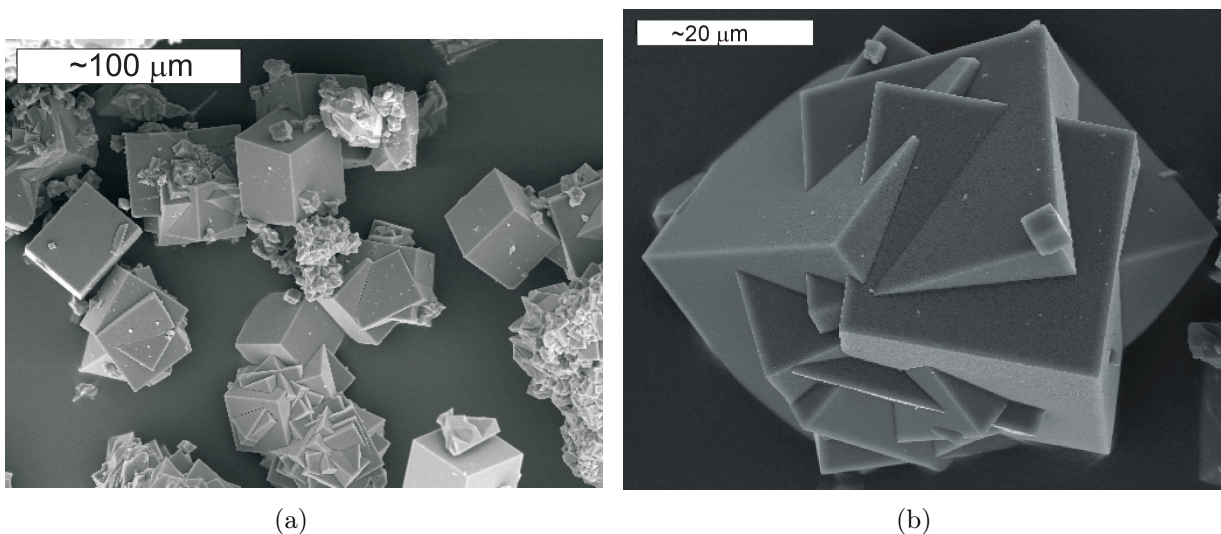
Figure 8: SEM pictures showing crystal growth defects observed in hydronium jarosite sample H3OS10, even though sample H3OS10 returned 100% Fe coverage. The differing reaction kinetics involved through the introduction of MeOH into the solvent produces distortions in morphology, severe changes are shown in Figures 4 and 5

is no suggestion that Fe^{3+} ions have been reduced to Fe^{2+} through the oxidation of MeOH, because as shown in this work the hydronium jarosite structure is not that tolerant to Fe vacancies and a charge disparity amounts to a Fe vacancy. Work on the formation mechanisms for jarosites[43] highlight that Fe^{2+} ions do not lead to the formation of hydronium jarosite, yet do so for the non-hydronium jarosites.[4] Likewise no diffraction data has shown the existence of Fe^{2+} oxy-hydroxy sulphate species in this work.

The non-hydronium jarosite structure appears to be more robust against Fe vacancy and can sustain losses up to 20%, than the hydronium jarosites. Surprisingly, though it appears that Fe occupation has little influence over the magnetism. Irrespective of the Fe content the magnetic transitions temperatures show two transitions for high A-site content, reducing to a single magnetic transition at a lower temperature which occurs with increasing H_3O^+ occupation in the A-site. This clearly demonstrates that it is the A-site which determines the nature and temperature of the magnetic transition. The hydronium ion has the largest a parameter for the jarosites[8] and it is the slight structural differences from the incorporation of the hydronium ion that is key to explaining the magnetic behaviour.
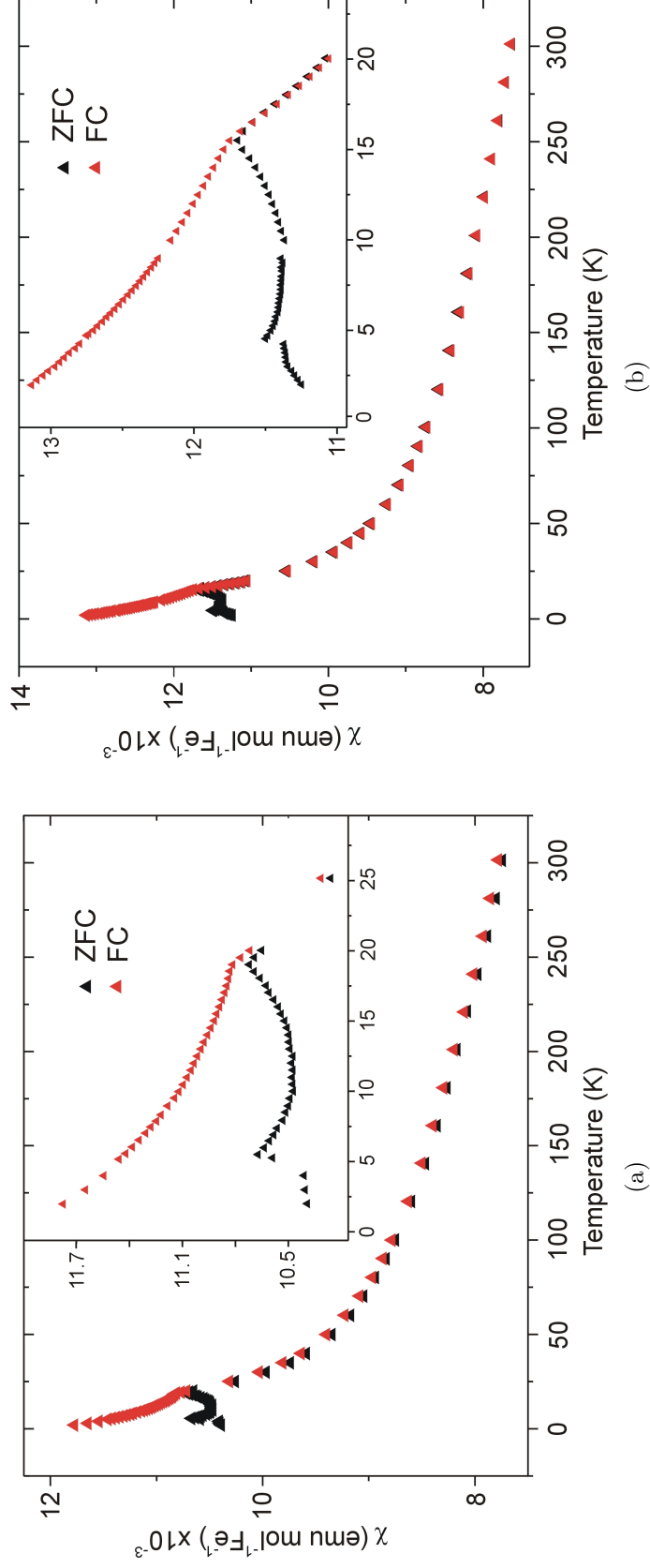
5   Acknowledgments

Figure 9: (a) and (b) zero field cooled (ZFC) and field cooled (FC) measurements of the magnetic susceptibility in a 100 Oe applied field from 2–300K. (a) is sample H3OS9, T_g=18.80K; and (b) is sample H3O024, T_g=15.69K. These two samples have relatively high values of T_g s and minimal Fe deficiencies. The inserts show an expansion of the region where the spin glass freezing transition occurs. The discontinuity seen in the ZFC below ~5K is from the sample having been temporarily warmed as small temperature fluctuations occur when the sample is cooled below 5K. Both these samples show distinct separation between ZFC and FC measurements. The FC susceptibility at 2K is slightly greater for sample H3O024 than for H3OS9.
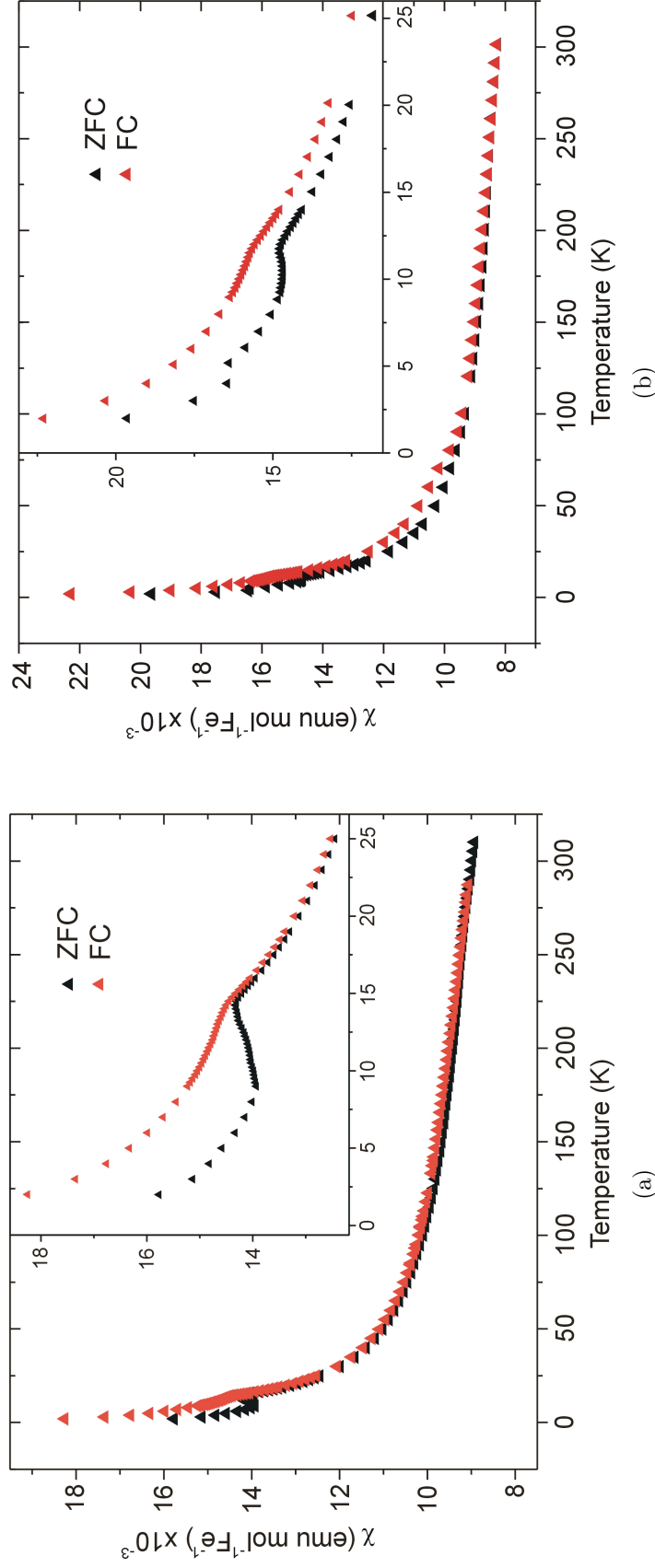
Figure 10: (a) and (b) show zero field cooled (ZFC) and field cooled (FC) measurements of the magnetic susceptibility in a 100 Oe applied field from 2–300K. (a) is sample H3OS34, T_g=13.85K. (b) is sample H3OS36, T_g=11.53K. These two samples have low values of T_g s and show a Fe deficiency. The inserts show an expansion of the region where the spin glass freezing transition occurs. The discontinuity seen in the ZFC below ~5K is from the sample having been temporarily warmed as small temperature fluctuations occur when the sample is cooled below 5K. Both these samples show a less distinct separation between ZFC and FC measurements as the super paramagnetic background increases. The spin glass transition for sample H3OS36 and H3OS9 measurements as the super paramagnetic background increases. The spin glass transition for sample H3OS24 and H3OS9. becomes smeared from the raised background.

Sciences) for obtaining the powder diffraction patterns.

References

[1] Anderson, P. W.; *Science,* **1987**, 235, 1196 .

[2] Singer, P. C.; Stumm, W.; *Science* **1970**, 167, 1121.

[3] Jambor, J. L. ; Nordstrom, D. K.; and Alpers, C. N., *Rev. Mineral Geochem,* **2000**, 40, 303.

[4] Sasaki, K.; Konno, H.; *Can. Mineral.* **2000**, 38, 45.

[5] Sasaki, K.; *Journal of the Mineralogical Scoiety of Japan,* **1997**, 26, 47.

[6] Smith, A. M. L.; Thesis: *Mechanisms and Products of the Contaminant Element-Bearing Jarosites,* University of London, **2004**,

[7] Lazaroff, N.; Sigal, W.; Wasserman, A., *Appl. Environ. Microb.,* **1982**, 43, 924.

[8] Dutrizac, J. E.; Kaiman, S.; *Can. Mineral.,* **1976**, 14, 151.

[9] Gray, N. F.; *Environ. Geol.,* **1996** 27, 358.

[10] Dutrizac, J. E.; *Metall Mater Trans B,* **1983**, 14, 531.

[11] Dutrizac, J. E.; Jambor, J. L.; *Reviews in Mineralogy and Geochemistry,* **2000**, 40, 405.

[12] Kubisz, J.; *Mineralogia Polonica,* **1970**, 1, 47.

[13] Dutrizac, J. E.; Chen, T. T.; *Metall Mater Trans B,* **2005**, 36, 33.

[14] Earle, S. A.; Ramirez, A. P.; Cava, R. J.; *Physica B,* **1999**, 262, 199.

[15] Wills, A. S.; Harrison, A., *J. Chem. Soc. Faraday T* **1996**, 92, 2161.

[16] Wills, A. S.; Oakley, G. S.; Visser, D.; Frunzke, J.; Harrison, A.; Andersen, K. H., *Phys. Rev. B* **2001**, 6409, 094436.

[17] Greedan, J. E., *J. Mater. Chem.* **2001**, 11, 37.

[18] Grohol, D.; Nocera, D. G.; Papoutsakis, D.; *Phys. Rev. B,* **2003**, 67, 064401.

[19] Chandra P.; Coleman P.; *Phys. Rev. Lett.,* **1991**, 66, 100.

[20] Wills, A. S.; Dupuis, V.; Vincent, E.; Hammann, J.; Calemczuk, R.;? **2000**, 62, R9264.

[21] Wills, A. S.; Harrison A.; Mentink, S. A. M.; Mason, T. E.; Tun, Z.; *Europhys. Lett.* **1998**, 42, 325.

[22] Inami, T.; Maegawa, S.; Takano, M., *J. Magn. Magn. Mater.* **1998**, 177, 752.

[23] Wills, A. S.; *Can. J. Phys.*, **2001**, 79, 1501.

[24] Wills, A. S.; *Phys. Rev. B*, **2001**, 6305, 064430.

[25] Grohol, D.; Matan, K.; Cho, J.-Y.; Lee, S.-H.; Lynn, J. W.; Nocera, D. G.; Lee, Y. S., *Nat. Mater.* **2005**, 4, 323.

[26] Wills, A. S.; Harrison A.; Ritter, C.; Smith, R. I., *Phys. Rev. B* **2000**, 61 6156.

[27] Elhajal, M.; Canals, B.; Lacroix, C.; **2002**, 66, 014422.

[28] Bekhechi, S.; Southern, B. W., *Phys. Rev. B*, **2003**, 67, 144403.

[29] Mydosh, J. A.; Spin Glasses: An Experimental Introduction *Taylor and Francis* **1993**

[30] Panagopoulos, C.; Majoros, M.; Nishizaki, T.; Iwasaki, H.; *Phys. Rev. Lett.*, **2006**, 96, 047002.

[31] Onuchic, J. N.; Luthey-Schulten, Z.; Wolynes, P. G.; *Annu. Rev. Phys. Chem.* **1997** 48, 545.

[32] Yildirim T.;Harris, A. B.; *Phys. Rev. B*, **2006**, 73, 214446.

[33] Gasharova B.; Gottlicher J.; Becker U.;, *Chem. Geol.*, **2004**, 215, 499.

[34] Shimizu S.; Hamada H.; *Angew. Chem. Int. Ed.*, **1999**, 38, 2725.

[35] Grohol, D.; Nocera, D. G., *J. Mater. Chem.* **2007**, 19, 3061.

[36] Ziff R. M.; Suding P. N.; *J. Phys. A: Math. Gen.* **1997**, 30, 5351.

[37] Ziff R. M.; Sapoval B.; *J. Phys. A: Math. Gen.* **1986**, 18, L1169.

[38] Smith, A. M. L.; Hudson-Edwards, K. A.; Dubbin, W. E.; Wright, K.; *Appl. Geochem.*, **2006**, 21, 1251.

[39] Ramirez, A.P.; Espionosa G. P.; Cooper, A. S.; *Phys. Rev. Lett.* **1990**, 64, 2070.

[40] Mendels, P.; Olariu, A.; Bert, F.; Bono, D.; Limot, L.; Collin, G.; Ueland, B.; Schiffer, P.; Cava, R. J.; Blanchard, N.; Duc, F.; Trombe, J. C., *Journal Of Physics-Condensed Matter*, **2007**, 19, 145224.

[41] Ripmeester, J. A.; Ratcliffe, C. I.; Dutrizac, J. E.; Jambor, J. L.; *Can. Mineral.*, **1986**, 24, 435,

[42] Drazin, P. G.; Johnson R. S.; Solitons: an Introduction *Cambridge University Press* **1989**

[43] Bisson W.; Wills, A. S., *Zeitschrift fur Kristallographie*, **2008**, in press.